Broadband Linear-to-Circular Polarization Conversion Enabled by Birefringent Off-Resonance Reflective Metasurfaces

Chun-Chieh Chang,[1] Zhexin Zhao,[2] Dongfang Li,[1] Antoinette J. Taylor,[3] Shanhui Fan,[2] and Hou-Tong Chen[1,*]
[1]*Center for Integrated Nanotechnologies, Los Alamos National Laboratory, Los Alamos, New Mexico 87545, USA*
[2]*E. L. Ginzton Laboratory, Department of Electrical Engineering, Stanford University, Stanford, California 94305, USA*
[3]*Associate Laboratory Director for Physical Sciences, Los Alamos National Laboratory, Los Alamos, New Mexico 87545, USA*

(Received 23 December 2018; published 4 December 2019)

Due to the scarcity of circular polarization light sources, linear-to-circular polarization conversion is required to generate circularly polarized light for a variety of applications. Despite significant past efforts, broadband linear-to-circular polarization conversion remains elusive particularly in the terahertz and midinfrared frequency ranges. Here we propose a novel mechanism based on coupled mode theory, and experimentally demonstrate at terahertz frequencies that highly efficient (power conversion efficiency approaching unity) and ultrabroadband (fractional bandwidth up to 80%) linear-to-circular polarization conversion can be accomplished by the judicious design of birefringent metasurfaces. The underlying mechanism operates in the frequency range between well separated resonances, and relies upon the phase response of these resonances away from the resonant frequencies, as well as the balance of the resonant and nonresonant channels. This mechanism is applicable for any operating frequencies from microwave to visible. The present Letter potentially opens a wide range of opportunities in wireless communications, spectroscopy, and emergent quantum materials research where circularly polarized light is desired.

DOI: 10.1103/PhysRevLett.123.237401

The polarization state is one of the intrinsic properties of light and circularly polarized light finds a wide range of applications such as circular dichroism spectroscopy [1], all optical magnetic recording [2], sensing [3], materials characterization [4,5], and wireless communications [6]. Typical coherent light sources are linearly polarized, making linear-to-circular polarization conversion the practical way to generate circularly polarized light. Wave plates based on a single birefringent material plate are narrow band; stacking multiple birefringent plates with carefully arranged thicknesses and orientations can expand the operational bandwidth [7,8], but the design and fabrication become more complex. Although achromatic polarization conversion can be realized by using total internal reflection in prisms such as Fresnel rhombs [9], the bulky size makes it difficult to miniaturize and integrate in optical systems. These issues pose further challenges to the broadband modulation of circular polarization states, e.g., for circular dichroism spectroscopy, where linear-to-circular polarization conversion is a prerequisite. Particularly at terahertz (THz) frequencies, photoelastic modulators [10] conventionally used in the optical regime are infeasible as the increasing wavelengths require the prohibitively high electromechanical driving of the photoelastic materials to induce sufficiently large birefringence and phase delay between the two orthogonal linear polarization components.

Metamaterials and metasurfaces have demonstrated exotic properties in controlling light propagation as well as the amplitude, phase, and polarization state [11]. Chiral metamaterials may function as circular polarizers [12,13], but at least half of the incident power is lost. A variety of anisotropic metamaterials and metasurfaces have enabled linear-to-circular polarization conversion [14–22], with issues remaining such as limited bandwidth, high insertion losses, and angle dispersion. Form birefringence in subwavelength gratings has also received significant attention during the past two decades to expand the operational bandwidth [23–25]; however, shortcomings such as the requirements of thick structures and high values of refractive index have prevented them from wider applications. In this Letter, we first theoretically propose a novel mechanism based on coupled mode theory to enable ultrabroadband linear-to-circular polarization conversion. In simulations and experiments, we validate this mechanism by the judicious design of resonances in birefringent reflective metasurfaces that can tailor the off-resonance phase dispersion to achieve arbitrary and constant phase difference between the two orthogonal linear polarization components. We present two metasurface structures operating either under normal incidence or at 45° incidence angle, experimentally demonstrating the fractional bandwidth of 3 dB axial ratio as broad as 62% and 80%, respectively, with conversion efficiencies approaching unity. We further show that the proposed approach is generally applicable from microwave to visible by simply scaling the metasurface structure.

Assuming nondispersive refractive indices, the narrow band operation of a single-plate birefringent wave plate is

essentially due to the linear phase dispersion with different slopes for the extraordinary and ordinary waves. The relative phase delay is proportional to frequency and therefore specific values of phase delay (e.g., for half-wave and quarter-wave plates) can be only obtained at some discrete frequencies, unless using birefringent materials with appropriate dispersion (which are difficult to find) to compensate such a frequency dependence. This issue can be potentially circumvented by deliberately introducing resonances to tailor the phase dispersion. Assuming a reflective surface with birefringent structures, for one linear polarization field component (e.g., $E_\perp$, consistent with the notation in the following simulations and experiments), it is nonresonant and its frequency-dependent reflection coefficient can be simply described as

$$\tilde{r}_\perp \equiv r_\perp(\nu)e^{i\phi_\perp(\nu)} = e^{i(b_\perp\nu+\phi_0)}, \tag{1}$$

where $r_\perp$ is the amplitude reflectivity and has been assumed to be unity [see Fig. 1(a)], ν is frequency, $b_\perp$ is a constant representing the nonresonant linear phase dispersion, and ϕ_0 is frequency independent and determined by the nature of the surface. Obviously $\phi_\perp$ has a trivial linear dispersion as shown in Fig. 1(b). For the orthogonal linear polarization field component ($E_\parallel$), the surface supports one or more resonant modes, and here we assume two well-separated resonant modes at ν_1 and ν_2 (i.e., their coupling is negligible). The reflection coefficient can be described using coupled mode theory [26–28]:

$$\begin{aligned}\tilde{r}_\parallel(\nu) &\equiv r_\parallel(\nu)e^{i\phi_\parallel(\nu)} \\ &= \left(\tilde{r}_{\rm nr} + \frac{\tilde{d}_1^2}{-i(\nu-\nu_1)+\gamma_1} + \frac{\tilde{d}_2^2}{-i(\nu-\nu_2)+\gamma_2}\right)e^{ib_\parallel\nu}.\end{aligned} \tag{2}$$

Here $\tilde{r}_{\rm nr}$ is the complex reflection coefficient of the nonresonant channel, $b_\parallel$ is also a constant similarly defined as in $b_\perp$, and $\tilde{d}_j$ and γ_j ($j = 1, 2$) are the complex coupling coefficient and decay rate, respectively, of the two resonant

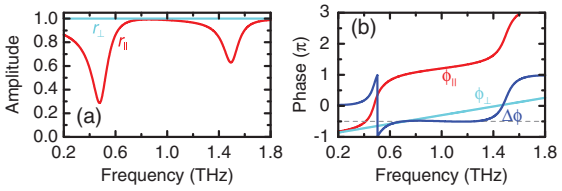

FIG. 1. (a) Amplitude reflectivity and (b) phase spectra along with the (wrapped) phase difference $\Delta\phi \equiv \phi_\parallel - \phi_\perp$ of a hypothetical reflective surface with birefringent properties following Eqs. (1) and (2) and using a set of parameters (based on the unit of THz for frequency): $\tilde{r}_{\rm nr} = 0.98e^{i(0.95\pi)}$, $\tilde{d}_1 = 0.36 + i0.025$, $\tilde{d}_2 = 0.36 - i0.045$, $\nu_1 = 0.5$, $\nu_2 = 1.5$, $\gamma_1 = 0.1$, $\gamma_2 = 0.08$, $b_\parallel = 0.8$, $b_\perp = 2.2$, and $\phi_0 = \pi$.

modes. The choice of parameters in Eq. (2) allows two underdamped resonances represented by the dips of $r_\parallel$ in Fig. 1(a) and the corresponding strongly nonlinear dispersion of $\phi_\parallel$ in Fig. 1(b). We find that the first resonance at 0.5 THz lifts the phase dispersion curve with an amount determined by the properties of the resonance. Importantly, the right-side tail of the first resonance and the left-side tail of the second resonance (at 1.5 THz) enforce a close-to-linear phase dispersion at off-resonance frequencies between the two resonances. The slope of $\phi_\parallel$ is determined by the properties of and the separation between the two resonances, and it can be smaller or greater than, or equal to the slope of $\phi_\perp$ as we desire. In the latter case the relative phase delay $\Delta\phi \equiv \phi_\parallel - \phi_\perp$ will be a constant but can be tuned to an arbitrary value at frequencies between the two resonances. The simultaneous high amplitude reflectivity and desired phase dispersion at off-resonance frequencies, as shown in Fig. 1, will allow us to accomplish broadband linear-to-circular polarization conversion.

One approach to realize underdamped resonances is using a Fabry-Pérot-like cavity in metal-dielectric-metal metasurfaces [29–34]. In Fig. 2(a) we illustrate the schematic of the unit cell of a metasurface structure used in our demonstration, consisting of a rectangular silicon pillar ($L = 110$ μm, $w = 16$ μm, $h = 44$ μm) created directly on a high-resistivity silicon substrate, with 10-nm-thick titanium and 200-nm-thick gold films coated on the top surface and on the rest of substrate surface, but not on the sidewall of the pillar. The complementary bilayer metallic structure is periodic with a square lattice ($P = 100$ μm), as shown in Figs. 2(b) and 2(c) for the scanning electron microscopy (SEM) images of a fabricated sample (see Supplemental Material for sample preparation [35]). The considerations of using such a metasurface structure include the following: (i) it provides a desirable birefringent background reflection as inferred by $b_\parallel \neq b_\perp$; (ii) $E_\perp$ interacts only very weakly with the cut-wire resonators, and it is mostly reflected directly by the ground plane with a close-to-linear phase dispersion; and (iii) for $E_\parallel$, both the resonator array and the ground plane (with slots) are expected to exhibit significant reflection thereby forming a Fabry-Pérot-like cavity, and the low loss in the high-resistivity silicon pillars enables underdamped resonances. Such a metasurface will fulfill the requirements of the proposed concept of broadband linear-to-circular polarization conversion based on the coupled mode theory.

The metasurface geometric parameters are determined through full-wave numerical simulations (see Supplemental Material [35]), with amplitude reflectivity and phase spectra shown in Figs. 2(d) and 2(e), respectively, for both the parallel and perpendicular field components. The fabricated metasurface sample with these geometric parameters ($P = 100$ μm, $L = 110$ μm, $w = 16$ μm, and $h = 44$ μm) is characterized using THz time-domain spectroscopy (THz-TDS) [36,37] under normal incidence, with a gold mirror on

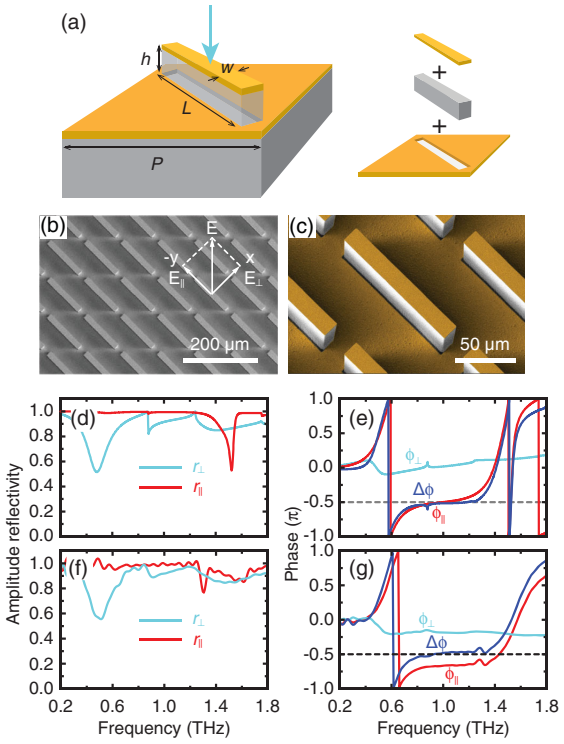

FIG. 2. (a) Schematic of the unit cell of a metasurface structure to realize broadband linear-to-circular polarization conversion. Inset: displacing the metallic structures from the dielectric pillar to reveal the structural details. (b) SEM micrograph of a fabricated metasurface sample, and (c) its false color close-up view. The normally incident THz radiation E is linearly polarized at 45° with respect to the major principal axis. (d) Numerically simulated amplitude reflectivity and (e) phase spectra for the parallel ($r_{\parallel}$ and $\phi_{\parallel}$) and perpendicular ($r_{\perp}$ and $\phi_{\perp}$) field components, along with their phase difference $\Delta\phi$. (f) Experimentally measured amplitude reflectivity and (g) phase spectra and their difference.

a similar substrate used as the reference (see the Supplemental Material for measurements and data analysis [35]). The experimental results are shown in Figs. 2(f) and 2(g), exhibiting excellent agreement with the numerical simulations.

For $E_{\parallel}$, the first Fabry-Pérot resonance is at ~0.6 THz and mainly determined by the values of L and P (see the Supplemental Material for interference model calculations [35]), as indicated by the strongly nonlinear dispersion of $\phi_{\parallel}$ shown in Figs. 2(e) and 2(g), although in Figs. 2(d) and 2(f) the amplitude reflectivity $r_{\parallel}$ exhibits only a negligible resonant dip at this frequency. The second Fabry-Pérot resonance occurs at ~1.5 THz as indicated by the significant resonant reflection dip and strongly nonlinear phase dispersion. The value of w mainly determines the birefringent phase dispersion and h determines the phase difference (see the Supplemental Material [35]). Both simulations and experiments show high amplitude reflectivity and nearly constant $\Delta\phi = -\pi/2$ over a broad off-resonance frequency range between the two Fabry-Pérot resonances, thanks to the linear and parallel dispersion of $\phi_{\parallel}$ and $\phi_{\perp}$, in accordance with the coupled mode analysis. The simulated and measured complex reflection coefficients can be used to retrieve the circular polarization states when the incident THz waves are linearly polarized at 45° with respect to the metasurface major principal axis as indicated in Fig. 2(b). We find in Fig. 3(a) that the reflection shows almost purely right-handed circular polarization with experimental power conversion efficiency mostly $R_R > 90\%$ (and $R_L \sim 0$) except the resonant dip at the high frequency end. In Fig. 3(b) we plot the experimentally obtained axial ratio of the reflected THz waves, which is less than 3 dB from 0.73 to 1.39 THz, corresponding to a 3 dB fractional bandwidth FBW = 62%. In another fabricated metasurface device with $L = 120$ μm, we accomplish a 3 dB FBW = 71% (see the Supplemental Material [35]). It is straightforward that simply rotating the metasurface or the incident linear polarization by 90° will result in the broadband conversion to left-handed circular polarization.

The presented metasurface structure is mechanically robust and simple to fabricate. Due to the metasurface structure design and fabrication procedure, however, the ground plane contains rectangular slots, which introduce the undesirable features in the spectra of $r_{\perp}$ as shown in Fig. 2, caused by various plasmonic modes from either individual or array of slots. This issue, although not severe, can be circumvented by using a continuous ground plane, as schematically illustrated in Fig. 4(a). It consists of a rectangular dielectric pillar formed by standard photolithography methods using SU-8 photoresist, sitting on a continuous gold reflector and coated with 3-nm-thick titanium and 220-nm-thick gold films on its top surface but not on its sidewall. Under normal incidence, the performance improvement is validated by numerical simulations with results shown in the Supplemental Material [35]. Compared with the structure in Fig. 2, this structure has additional material loss since SU-8, being a polymer, has more loss as compared to single crystalline silicon in the THz wavelength range.

The normal incidence is not a necessary requirement for the coupled mode theory and the proposed metasurface

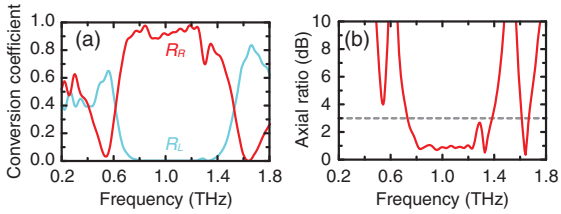

FIG. 3. (a) The retrieved circular polarization states from experimentally measured reflection data when the normally incident THz waves are linearly polarized at 45° with respect to the metasurface major principal axis. (b) Axial ratio of the reflected THz waves calculated from experimental measurements.

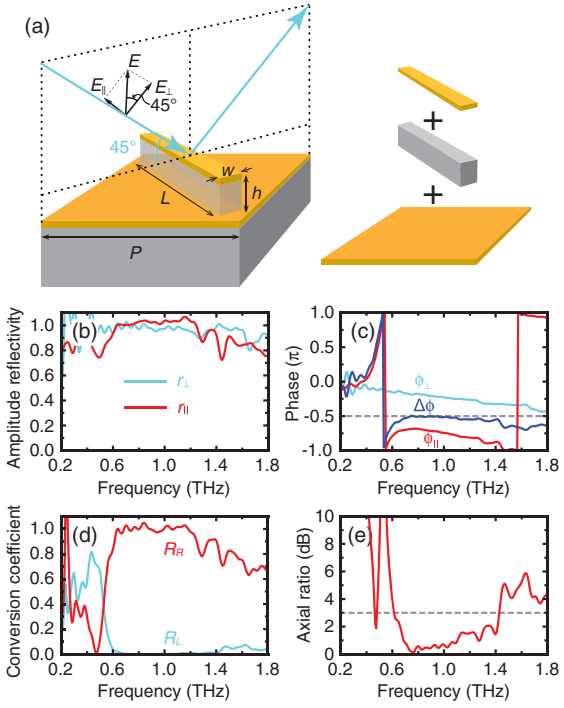

FIG. 4. (a) Schematic of the unit cell of a metasurface structure for broadband linear-to-circular polarization conversion at 45° incidence angle. Inset: displacing the metallic structures to reveal the unit cell details. (b) Experimentally measured amplitude reflectivity and (c) phase spectra for the parallel ($r_{\parallel}$ and $\phi_{\parallel}$) and perpendicular ($r_{\perp}$ and $\phi_{\perp}$) field components, along with their phase difference $\Delta\phi$. (d) The retrieved circular polarization states when the incident THz waves are linearly polarized at 45° with respect to the plane of incidence. (e) Axial ratio of the reflected THz waves.

structures. Indeed, oblique incidence (e.g., at 45° incidence angle) is more convenient for some practical applications when using reflective metasurfaces. We have numerically verified that both metasurface structures shown in Figs. 2(a) and 4(a) can operate at 45° incidence angle when their geometric dimensions are appropriately tuned (see the Supplemental Material [35]). In experiments, we have fabricated the metasurface structure shown in Fig. 4(a) (also see SEM images in the Supplemental Material [35] for a fabricated sample), with $P = 140$ μm, $L = 170$ μm, $w = 22$ μm, and $h = 48$ μm. The reflection properties of the metasurface sample are characterized using THz-TDS at a 45° incidence angle, where the plane of incidence is perpendicular to the metasurface major principal axis, as schematically illustrated in Fig. 4(a).

The experimental measurements (and numerical simulations) show that $\tilde{r}_{\parallel}$ exhibits an underdamped Fabry-Pérot resonance at 0.5 THz [see Figs. 4(b) and 4(c)]. The second Fabry-Pérot resonance near 1.44 THz, on the other hand, exhibits overdamped characteristics with a small Lorentzian phase dispersion [see $\phi_{\parallel}$ in Fig. 4(c)] due to the increasing loss within the SU-8 pillars (typical loss tangent between 0.05–0.10, here we use 0.07 in simulations) [38]. This change of characteristics in the second resonance, however, seems to have minimal effects on retaining the parallel linear phase dispersion and thereby constant phase difference $\Delta\phi = -\pi/2$, as shown in Fig. 4(c) for the phase spectra measured in experiments. This suggests that, when using coupled mode theory, the first underdamped resonance plays the most important role in our case, and there is some design freedom in choosing the characteristics of resonances in realizing and even further broadening the broadband linear-to-circular polarization conversion. The retrieved circular polarization states are shown in Fig. 4(d) when the incident THz waves are linearly polarized at 45° with respect to the plane of incidence, revealing almost purely right-handed circular polarization with power conversion efficiency near unity. In Fig. 4(e) we find that the obtained axial ratio is less than 3 dB from 0.61 to 1.43 THz, corresponding to a remarkably broad 3 dB FBW = 80%.

The off-resonance operation of the presented metasurfaces makes them scalable to operate at any relevant frequencies ranging from microwave to visible. Numerical simulations have been performed to validate this scalability at near-infrared and visible wavelengths despite the increase of metallic losses, using the same metasurface structure shown in Fig. 4(a) with geometric parameters scaled to $P = 200$ nm, $L = 230$ nm, $w = 40$ nm, and $h = 100$ nm, which are all feasible for standard nano-fabrication. The thickness of the gold films is 30 nm, and the complex permittivity can be derived from Drude model [39], but here it is taken from Johnson and Christy [40]. The dielectric pillar is made of silicon dioxide with dielectric function taken from Malitson [41]. The simulated amplitude

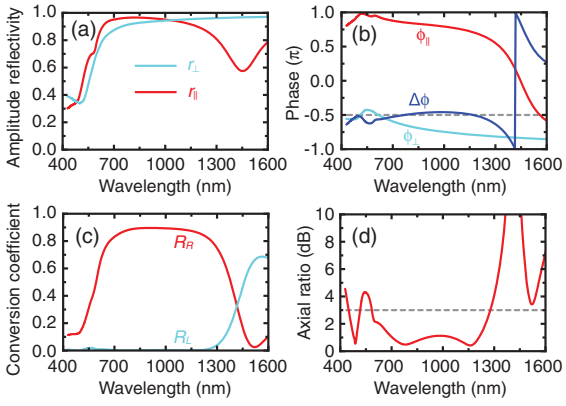

FIG. 5. (a) Numerically simulated amplitude reflectivity and (b) phase spectra along with the phase difference $\Delta\phi$ of a reflective metasurface under 45° incidence angle and operating at near-infrared and visible wavelengths. (c) The retrieved circular polarization states when the incident light is linearly polarized at 45° with respect to the plane of incidence. (d) Axial ratio of the reflected light showing a 3 dB fractional bandwidth of 75%.

reflectivity and phase spectra are shown in Figs. 5(a) and 5(b), respectively. For $E_{\|}$, the first Fabry-Pérot resonance occurs at $\lambda = 1450$ nm, which is a very robust underdamped resonance. The second Fabry-Pérot resonance seems to occur at $\lambda = 570$ nm, exhibiting a small Lorenzian-type phase dispersion due to the increasing metallic loss. Between the two resonances, the amplitude reflectivity is high for both field components, and their phase dispersion is close to linear and parallel with each other, providing a nearly constant phase difference $\Delta\phi = -\pi/2$. The circular polarization states of the reflected light are retrieved and shown in Fig. 5(c), revealing a linear-to-circular polarization power conversion efficiency R_R mostly between 85% and 90% (and $R_L \sim 0$), and accomplishing a 3 dB fractional bandwidth of 75% (from $\lambda = 1278$ nm to 584 nm) as shown in Fig. 5(d).

In summary, based on coupled mode theory, we have proposed and experimentally demonstrated off-resonance reflective metasurfaces accomplishing linear-to-circular polarization conversion in the THz frequency range with near-unity power conversion efficiencies and over a full octave bandwidth. We present two metasurface designs operating either under normal incidence or at 45° incidence angle, making such broadband reflective metasurface quarter-wave plates suitable for practical applications. The off-resonance operation overcomes the loss issues associated with typical resonant metasurfaces, thereby scalable to operate at other wavelengths ranging from microwave to visible. The accomplished remarkable bandwidth (FBW $\sim 80\%$) is much broader than previous demonstrations using anisotropic gap-plasmon resonators (FBW $\sim 20\%$) [18] and L-shaped resonators with a back reflector (FBW $\sim 30\%$) [22], which exploited a different mechanism with resonant eigenmodes for both orthogonal field components. Other constant $\Delta\phi$ values can also be realized by tailoring the metasurface structure, including $\Delta\phi = \pi$ for ultrabroadband linear polarization rotation of 90° [32]. We expect that this work will stimulate the study of emergent quantum materials such as topological insulators and Weyl and Dirac semimetals [4,5] where circularly polarized high-intensity low-energy THz and midinfrared photons are ideal to investigate their rich physics. The capability of generating broadband circularly polarized THz waves is also highly desirable in free space THz wireless secure communications [6,42] and potentially enables THz circular dichroism spectroscopy which is of great importance in biochemistry [43,44].

We acknowledge partial support of the Los Alamos National Laboratory Laboratory-Directed Research and Development (LDRD) program. Z. Zhao and S. Fan acknowledge the support of the Department of Energy under Grant No. DE-FG02-07ER46426. This work was performed, in part, at the Center for Integrated Nanotechnologies, an Office of Science User Facility operated for the U.S. Department of Energy (DOE) Office of Science. Los Alamos National Laboratory, an affirmative action equal opportunity employer, is managed by Triad National Security, LLC for the U.S. Department of Energys NNSA, under Contract No. 89233218CNA000001.

C. C. C., Z. Z., and D. L. contributed equally to this work.

*chenht@lanl.gov

[1] S. Beychok, Science **154**, 1288 (1966).
[2] C. D. Stanciu, F. Hansteen, A. V. Kimel, A. Kirilyuk, A. Tsukamoto, A. Itoh, and T. Rasing, Phys. Rev. Lett. **99**, 047601 (2007).
[3] G. D. Lewis, D. L. Jordan, and P. J. Roberts, Appl. Opt. **38**, 3937 (1999).
[4] H. Yuan, X. Wang, B. Lian, H. Zhang, X. Fang, B. Shen, G. Xu, Y. Xu, S.-C. Zhang, H. Y. Hwang *et al.*, Nat. Nanotechnol. **9**, 851 (2014).
[5] Q. Ma, S.-Y. Xu, C.-K. Chan, C.-L. Zhang, G. Chang, Y. Lin, W. Xie, T. Palacios, H. Lin, S. Jia *et al.*, Nat. Phys. **13**, 842 (2017).
[6] S. X. Ta, I. Park, and R. W. Ziolkowski, IEEE Antennas Propag. Mag. **57**, 107 (2015).
[7] S. Pancharatnam, Proc. India Acad. Sci. A **41**, 137 (1955).
[8] J.-B. Masson and G. Gallot, Opt. Lett. **31**, 265 (2006).
[9] Y. Kawada, T. Yasuda, A. Nakanishi, K. Akiyama, K. Hakamata, and H. Takahashi, Opt. Lett. **39**, 2794 (2014).
[10] K. W. Hipps and G. A. Crosby, J. Phys. Chem. **83**, 555 (1979).
[11] H.-T. Chen, A. J. Taylor, and N. Yu, Rep. Prog. Phys. **79**, 076401 (2016).
[12] J. K. Gansel, M. Thiel, M. S. Rill, M. Decker, K. Bade, V. Saile, G. von Freymann, S. Linden, and M. Wegener, Science **325**, 1513 (2009).
[13] Y. Zhao, M. A. Belkin, and A. Alù, Nat. Commun. **3**, 870 (2012).
[14] X. G. Peralta, E. I. Smirnova, A. K. Azad, H.-T. Chen, A. J. Taylor, I. Brener, and J. F. O'Hara, Opt. Express **17**, 773 (2009).
[15] A. C. Strikwerda, K. Fan, H. Tao, D. V. Pilon, X. Zhang, and R. D. Averitt, Opt. Express **17**, 136 (2009).
[16] L. Q. Cong, N. N. Xu, J. Q. Gu, R. Singh, J. G. Han, and W. L. Zhang, Laser Photonics Rev. **8**, 626 (2014).
[17] J. M. Hao, Y. Yuan, L. X. Ran, T. Jiang, J. A. Kong, C. T. Chan, and L. Zhou, Phys. Rev. Lett. **99**, 063908 (2007).
[18] A. Pors and S. I. Bozhevolnyi, Opt. Express **21**, 2942 (2013).
[19] W. S. L. Lee, R. T. Ako, M. X. Low, M. Bhaskaran, S. Sriram, C. Fumeaux, and W. Withayachumnankul, Opt. Express **26**, 14392 (2018).
[20] Y. Jia, Y. Liu, W. Zhang, J. Wang, Y. Wang, S. Gong, and G. Liao, Opt. Mater. Express **8**, 597 (2018).
[21] N. Yu, F. Aieta, P. Genevet, M. A. Kats, Z. Gaburro, and F. Capasso, Nano Lett. **12**, 6328 (2012).
[22] S.-C. Jiang, X. Xiong, Y.-S. Hu, Y.-H. Hu, G.-B. Ma, R.-W. Peng, C. Sun, and M. Wang, Phys. Rev. X **4**, 021026 (2014).
[23] H. Kikuta, Y. Ohira, and K. Iwata, Appl. Opt. **36**, 1566 (1997).

[24] G. P. Nordin and P. C. Deguzman, Opt. Express **5**, 163 (1999).
[25] N. W. Roberts, T.-H. Chiou, N. J. Marshall, and T. W. Cronin, Nat. Photonics **3**, 641 (2009).
[26] S. Fan, W. Suh, and J. D. Joannopoulos, J. Opt. Soc. Am. A **20**, 569 (2003).
[27] W. Suh, Z. Wang, and S. Fan, IEEE J. Quantum Electron. **40**, 1511 (2004).
[28] Z. Miao, Q. Wu, X. Li, Q. He, K. Ding, Z. An, Y. Zhang, and L. Zhou, Phys. Rev. X **5**, 041027 (2015).
[29] H.-T. Chen, J. F. Zhou, J. F. O'Hara, F. Chen, A. K. Azad, and A. J. Taylor, Phys. Rev. Lett. **105**, 073901 (2010).
[30] H.-T. Chen, Opt. Express **20**, 7165 (2012).
[31] L. Huang, D. R. Chowdhury, S. Ramani, M. T. Reiten, S.-N. Luo, A. K. Azad, A. J. Taylor, and H.-T. Chen, Appl. Phys. Lett. **101**, 101102 (2012).
[32] N. K. Grady, J. E. Heyes, D. R. Chowdhury, Y. Zeng, M. T. Reiten, A. K. Azad, A. J. Taylor, D. A. R. Dalvit, and H.-T. Chen, Science **340**, 1304 (2013).
[33] L. Huang, C.-C. Chang, B. Zeng, J. Nogan, S.-N. Luo, A. J. Taylor, A. K. Azad, and H.-T. Chen, ACS Photonics **4**, 2111 (2017).
[34] C.-C. Chang, L. Huang, J. Nogan, and H.-T. Chen, APL Photonics **3**, 051602 (2018).
[35] See the Supplemental Material at http://link.aps.org/supplemental/10.1103/PhysRevLett.123.237401 for sample fabrication, geometric parameter dependence, numerical simulations, measurements, data analysis, and model calculations.
[36] D. Grischkowsky, S. Keiding, M. van Exter, and C. Fattinger, J. Opt. Soc. Am. B **7**, 2006 (1990).
[37] Q. Wu, M. Litz, and X. Zhang, Appl. Phys. Lett. **68**, 2924 (1996).
[38] N. Ghalichechian and K. Sertel, IEEE Antennas Wireless Propag. Lett. **14**, 723 (2015).
[39] M. A. Ordal, R. J. Bell, R. W. Alexander, L. L. Long, and M. R. Querry, Appl. Opt. **24**, 4493 (1985).
[40] P. B. Johnson and R. W. Christy, Phys. Rev. B **6**, 4370 (1972).
[41] I. H. Malitson, J. Opt. Soc. Am. **55**, 1205 (1965).
[42] J. Ma, R. Shrestha, J. Adelberg, C.-Y. Yeh, Z. Hossain, E. Knightly, J. M. Jornet, and D. M. Mittleman, Nature (London) **563**, 89 (2018).
[43] P. L. Polavarapu and G.-C. Chen, Appl. Spectrosc. **48**, 1410 (1994).
[44] J. Xu, G. J. Ramian, J. F. Galan, P. G. Savvidis, A. M. Scopatz, R. R. Birge, S. J. Allen, and K. W. Plaxco, Astrobiology **3**, 489 (2003).